Sub-Resolution Assist Feature Generation with Supervised Data Learning

Xiaoqing Xu *Student Member, IEEE*, Yibo Lin, Meng Li *Student Member, IEEE*, Tetsuaki Matsunawa *Member, IEEE*, Shigeki Nojima, Chikaaki Kodama *Senior Member, IEEE*, Toshiya Kotani, and David Z. Pan *Fellow, IEEE*

Abstract—**Sub-Resolution Assist Feature (SRAF) generation is a very important resolution enhancement technique to improve yield in modern semiconductor manufacturing process. Model-based and rule-based approaches are widely adopted in the semiconductor industry. The model-based SRAF generation can achieve a high accuracy but it is known to be time-consuming and it is hard to obtain consistent SRAFs on the same layout pattern configurations. The rule-based SRAF generation is highly technology dependent and it is becoming extremely difficult to render high-quality results in advanced technology nodes. This paper proposes supervised data learning techniques for fast yet consistent SRAF generation with high-quality results. We first propose the constrained concentric circle with area sampling scheme for feature extraction. Illumination source symmetry-based feature compaction technique is further invented to reduce the training data set size and achieve consistent SRAF predictions. Using accurate model-based SRAFs as training data, classification models based on logistic regression and support vector machine are calibrated for SRAF predictions. Moreover, the probability maximum prediction is proposed to generate manufacturing-friendly SRAFs with a greedy simplification scheme. We compare support vector machine and logistic regression models by embedding into an entire mask optimization flow, where the support vector machine model obtains better lithographic performance. Experimental results demonstrate that, compared with the commercial Calibre tool, supervised data learning techniques for SRAF generation obtain significant speed up ($>$3X for a $100um^2$ layout clip) and comparable lithographic performance in terms of edge placement error and process variation band.**

Keywords—*Sub-Resolution Assist Feature, Supervised Learning, Logistic Regression, Support Vector Classification*

I. INTRODUCTION

As the technology node continues scaling down, the $193nm$ wavelength photolithography with low $k1$ value is the mainstream technique to achieve smaller feature size. However, low image contrast and complex target pattern shapes make it extremely difficult for low-$k1$ lithography to obtain acceptable lithographic process windows [2]. Besides the design for manufacturability techniques, like multiple patterning and litho-friendly layout design, mask optimization through resolution enhancement techniques (RETs) remains as the key strategy
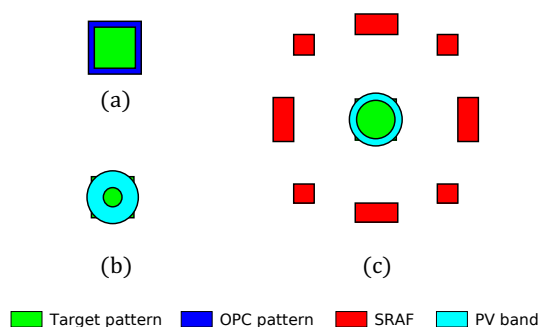
Fig. 1: (a) An isolated contact, (b) printing with OPC, (c) printing with SRAF generation and OPC.

to improve the lithographic process window and the yield of the volume production in advanced technology nodes [3]–[7]. Major RETs include source mask co-optimization, sub-resolution assist feature (SRAF) generation and optical proximity correction (OPC). Among them, the SRAF generation is particularly important to improve the lithographic process window of target patterns. The key physical mechanism behind is that, without printing themselves, the small SRAF patterns would deliver light to the positions of target patterns at proper phase so that the printing of target patterns will be more robust to the lithographic variations. The lithographic process window is quantified with the process variation (PV) band area, which should be minimized to obtain a robust mask optimization solution. An example demonstrating the benefit of SRAF generation is shown in Fig. 1. An isolated target contact with the OPC pattern is shown in Fig. 1(a) and the target pattern is optimized only with OPC in Fig. 1(b), while the optimization in Fig. 1(c) is done with both SRAF generation and OPC. It can be clearly observed that much smaller PV band area is achieved in Fig. 1(c). Therefore, fast and high-quality SRAF generation is of great importance for the mask optimization.

Multiple SRAF generation approaches, including model-based and rule-based approaches, have been developed and widely used in standard mask optimization flows. The rule-based approach is widely adopted due to its fast execution time and acceptable performance for simple designs and regular target patterns [2], [8], [9]. However, the rule-based SRAF is hard to deal with complex two-dimension (2D) shapes as it requires significant engineering efforts to setup and maintain the rule table [8]. Model-based SRAF generation methods

can be divided into two categories based on the lithographic computations involved. One is to use simulated aerial images to seed the SRAF generation [10]–[13]. The other is to apply inverse lithography technology (ILT) and compute the image contour to guide the SRAF generation [14], [15]. Despite better lithographic performance and generalization capabilities compared to the rule-based approach, the model-based SRAF is known to be very time-consuming and it is difficult to achieve the same SRAFs around the same layout configurations, i.e. consistent SRAFs [2], [8].

Recently, supervised learning techniques have been introduced to the computational lithography domain, with applications to lithographic hotspot detection [16]–[20] and OPC [21]–[24]. The supervised data learning technique calibrates a mathematical model with respect to an objective from the training data set based on accurate lithographic computations. Then, the calibrated model can predict the objective values, like a hotspot or non-hotspot for the hotspot detection and the shifting distance of an edge segment for the OPC, on the testing data. The supervised learning technique usually demonstrates a trade-off between computational efforts and lithographic performance, which makes it particularly attractive for the SRAF generation problem. However, to the best of our knowledge, there is no prior art in applying the supervised learning techniques to the SRAF generation problem. In this work, we propose novel supervised data learning techniques for the SRAF generation. Our methodology can achieve fast yet consistent SRAFs with high-quality results in a 2D grid plane. Our main contributions are summarized as follows.

- Supervised data learning techniques are proposed for the SRAF generation, where a classification model is calibrated for SRAF predictions using model-based SRAFs as the training data.
- We propose a robust feature extraction scheme by adapting the concentric circle with area sampling considering SRAF-specific constraints. We further propose a novel feature compaction technique taking advantage of illumination source symmetry properties to reduce the training data size and improve the SRAF consistency.
- Support vector machine and logistic regression are calibrated for fast SRAF predictions. Different from conventional label predictions, we propose predictions with probability maxima in the 2D grid plane to generate manufacturing-friendly SRAFs.
- The supervised data learning-based framework for SRAF generation achieves significant speedup ($>$3X for a $100um^2$ layout clip) with competitive lithographic performance, compared with an industry strength model-based approach.

The rest of this paper is organized as follows. Section II introduces the standard mask optimization flow and related evaluation metrics. Section III gives the basic definitions and problem formulations. Section IV explains the details on the feature extraction/compaction and model calibration for logistic regression and support vector machine. Section V demonstrates SRAF generation from the classification model while accommodating the mask manufacturing rules. Section VI demonstrates the effectiveness of the proposed supervised data learning techniques with comprehensive results. Section VII concludes the paper and discusses the future research directions.

II. PRELIMINARIES

In this section, we introduce the standard mask optimization flow and further embed the supervised data learning-based SRAF generation into the flow. Related metrics are introduced to evaluate the performance of the SRAF generation.

A. Mask Optimization Flow

A standard mask optimization flow consists of several stages, including SRAF generation, OPC, mask manufacturing rule check (MRC) and lithography compliance check (LCC) as shown in Fig. 2(a) [2]. Depending on the outcome of MRC and LCC, iterative optimizations may be applied to achieve legal mask patterns. The MRC will check whether mask patterns satisfy a set of mask manufacturing rules. The LCC means lithography simulations are performed to check whether lithographic constraints are satisfied. In the stage of SRAF generation, small SRAFs will be added and isolated patterns on the mask will become dense patterns as shown in Fig. 1(b). During lithographic printing, SRAFs will not be printed themselves but will deliver light to the target patterns at a proper phase, which contributes to more robust printing of target patterns.
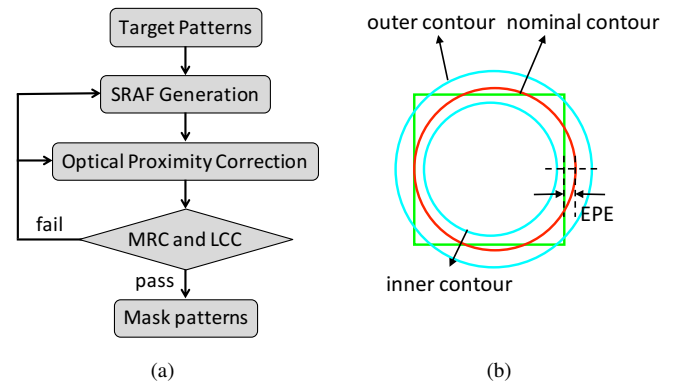

Fig. 2: Mask optimization: (a) a standard mask optimization flow, (b) lithography simulation contours under a set of {focus, dose} conditions.

In the next stage, OPC will shift the edges of OPC patterns to compensate for the optical proximity effects. Before achieving mask patterns, the MRC and LCC are performed to ensure that related lithographic constraints are satisfied. For the MRC, we assume the target patterns are MRC-clean and some typical mask manufacturing rules are applied to the SRAFs since this work mainly focuses on the SRAF generation. Typical mask manufacturing rules for SRAFs include maximum width (max_width) rule, minimum space (min_space) rule and maximum length (max_length) rule. The LCC will introduce a

lithographic process window involving a set of {focus, dose} conditions [25]. Lithography simulations at various conditions are performed to check whether the metrics, such as PV band and edge placement error (EPE), meet the criteria.

B. Evaluation Metrics

We introduce several metrics to evaluate the performance of mask optimization results. An example of lithography simulation results is shown in Fig. 2(b). Inner and outer contours are explicitly drawn to demonstrate the lithographic printing variations due to the imposed {focus, dose} conditions. Nominal contour represents the lithographic printing at the best {focus, dose} condition. To quantify the lithographic variations, we define PV band and EPE as follows.

Definition 1 (PV Band) *Given the lithography simulation contours at a set of {focus, dose} conditions, the process variation (PV) band is defined as the area between the outer contour and inner contour.*

Definition 2 (EPE) *Given the lithography simulation contour at the best {focus, dose} condition, i.e. nominal contour and a measurement point, the edge placement error (EPE) is defined as the distance between the target pattern contour and nominal contour.*

Thus, in Fig. 2(b), the area between the outer contour and inner contour is the PV band. A measurement point is drawn with a dashed line orthogonal to the vertical edge of the target pattern in Fig. 2(b) and the EPE can be explicitly quantified. The SRAF consistency is an important issue since it is closely related to the process variations on wafer [2]. Consistent SRAFs are preferred around the same target pattern configurations because different SRAFs lead to different OPC results, which potentially introduce extra process variations. An example on consistent SRAFs is that axial symmetric SRAFs should be generated for axial symmetric target patterns if annular illumination source has been used. We define the consistent SRAF generation as follows.

Definition 3 (Consistent SRAF generation) *Consistent SRAF generation means the same SRAF patterns should be generated for the same target layout configurations.*

III. PROBLEM FORMULATION

The supervised data learning-based SRAF generation works on a 2D grid plane with a specific grid size. The training data consists of a set of layout clips, where each layout clip includes a set of target patterns and model-based SRAFs. With the 2D grid plane and training layout patterns, training samples can be extracted at each grid point. We first define the SRAF label as follows.

Definition 4 (SRAF label) *Given model-based SRAFs on the 2D grid plane, the SRAF label of a grid is 1 or 0, where 1 denotes an SRAF is inserted at that grid and 0 vice versa.*

Specifically, a training data point includes a feature vector and an SRAF label. The feature vector represents the optical conditions of the grid point with respect to the target patterns.

After the training data preparation, we define the classification-based SRAF as follows.

Problem 1 (Classification-based SRAF) *Given the 2D grid plane and training patterns with model-based SRAFs, feature vectors and SRAF labels of all grid points are extracted and a classification model is calibrated to predict the SRAF insertion at each grid of testing patterns.*

In the testing phase, the classification model can predict the SRAF label at each grid point for testing patterns. Those grids with SRAF labeled as 1 can not directly be treated as the final SRAFs because further simplifications are needed to generate SRAFs while accommodating mask manufacturing rules. Thus, we define the SRAF generation as follows.

Problem 2 (SRAF Generation) *Given the classification model and test patterns, SRAFs are generated while accommodating the mask manufacturing rules.*

The supervised data-learning based framework for SRAF generation is demonstrated in Fig. 3, where Problem 1 is mainly related to the training phase and Problem 2 is associated with the testing phase. In particular, this work aims at supervised data learning-based techniques instead of traditional model-based or rule-based approaches. A complete mask optimization flow is obtained by combining the supervised data learning-based framework in Fig. 3 with other mask optimization stages shown in Fig. 2.
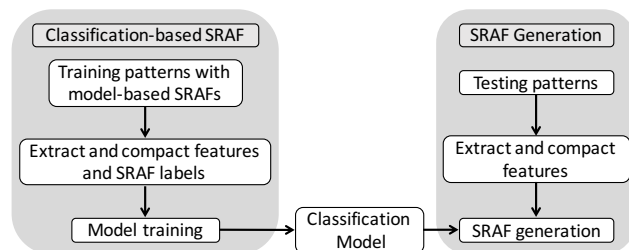

Fig. 3: Supervised data learning-based SRAF generation.

IV. CLASSIFICATION-BASED SRAF

A. Data Preparation

1) SRAF Label Extraction: Given training patterns with model-based SRAFs on a 2D grid plane, we need to extract the training data, including the SRAF label and feature vector for each grid. As shown in Fig. 4(a), a 2D grid plane is imposed on the target patterns and model-based SRAFs. The coordinates of each grid are determined by the pre-set grid size. An SRAF box is introduced at each grid to decide the SRAF label from model-based SRAFs. Specifically, the SRAF box is a rectangle and the size is a parameter, which could be different from the grid size. The SRAF label of the grid is 0 if no model-based SRAF covering the SRAF box on the grid. The SRAF label is 1 when there is a model-based SRAF covering the entire SRAF box area. Therefore, the grid size of the 2D grid plane decides the granularity of the training data extraction while the SRAF box provides an alternative control on the SRAF label

extraction accuracy. The SRAF label extraction will give a set of labels for all the grids, denoted as $\{y_0\}$.

In addition, an OPC region and an SRAF region are explicitly drawn in Fig. 4(a) to demonstrate SRAF-specific constraints. SRAF generation is not allowed in the OPC region since it is reserved for the OPC stage after the SRAF generation. Since the optical interference happens within some specific lithographic interaction window, the SRAF generation outside of the pre-determined SRAF region can be ignored. Both OPC region and SRAF region are created by expanding the edges of the target patterns by some specific distance. We define the distance of expansion for the OPC region and SRAF region as d_{opc} and d_{sraf}, respectively.
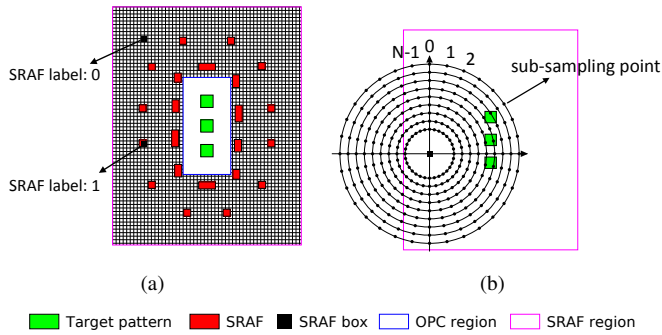

Fig. 4: (a) SRAF label extraction and sampling constraints, (b) CCCAS at one grid point.

2) Feature Extraction and Compaction: The layout feature extraction plays an important role in the classification model calibration and prediction. The SRAFs benefit the printing of target patterns by delivering light to the positions of target patterns at proper phase. Thus, we need a layout feature that represents this physical phenomenon. The concentric circle with area sampling is an ideal candidate since it represents the information related to the concentric propagation of diffracted light from mask patterns [23]. We adapt it to the constrained concentric circle with area sampling (CCCAS) by incorporating the OPC region and SRAF region constraints discussed in Section IV-A1. The CCCAS at one grid is illustrated in Fig. 4(b), where each circle centers at the grid and the minimum and maximum radius of the CCCAS are determined by d_{opc} and d_{sraf}, respectively. After transforming target patterns into the bitmap on the 2D plane, the CCCAS yields a $M \times N$ matrix, denoted as X_0, where M is the row number and N is the column number. As shown in Fig. 4(b), the column index of X_0 starts at the positive Y-axis with 0 and increases clockwise to $N-1$. The sub-sampling points, denoted as the black dots in Fig. 4(b), sharing the same angle to the origin are in the same column of X_0. The row index of X_0 starts with 0 at the circle with the smallest radius and increases to $M-1$ as the circle radius becomes larger. The sub-sampling points on the same circle are on the same row of X_0.

As discussed in Section II-B, the consistent SRAF generation is a very important issue, which means the same SRAFs will be generated surrounding the same target pattern config-

urations, i.e., the same optical conditions [8]. For example, in Fig. 5, the four grids are on axial symmetric positions of the grid plane with respect to the target patterns. If we assume the annular shape of the illumination source, the optical conditions of these four grids are the same and consistent SRAF generation scheme will give the same SRAF results. However, since the CCCAS at these four grids are different, denoted by different colors in Fig. 5, it is difficult for a classification model to achieve the same SRAF predictions. To achieve better SRAF consistency, we propose a novel feature compaction technique taking advantage of the illumination source symmetry. As shown in Fig. 5, this feature compaction technique transforms the CCCAS of symmetric grids into the CCCAS of the same grid, denoted as g, in the lower left of the grid plane. The sampling region of the grid (g) can be divided into four quadrants, i.e., I, II, III and IV. The target patterns mainly locate at the quadrant I of the sampling region of the grid (g), while target patterns mainly locate at different quadrants for other symmetric grids. For clearer explanations, we define the main quadrant as follows.

Definition 5 (Main Quadrant) *The main quadrant for a grid is defined as the quadrant of the CCCAS region where target patterns mainly locate.*

By flipping the CCCAS of other symmetric grids with X or Y-axis as shown in Fig. 5, target patterns will always locate at the quadrant I of the sampling regions for symmetric grids, which leads to the same CCCAS results. Then, the classification model will give consistent SRAF predictions for axial symmetric grids.
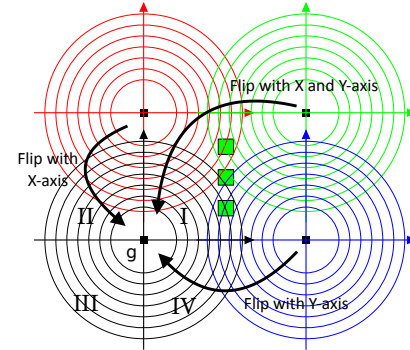

Fig. 5: Feature compaction based on symmetry.

The details of the feature compaction technique are explained in Algorithm 1. The 2D feature matrix from CCCAS contains the bitmap value at each sub-sampling point. The bitmap values of sub-sampling points within each quadrant of the sampling region correspond to a set of columns in the 2D feature matrix. Thus, the main quadrant should have the maximum summation of bitmap values at the 2D feature matrix. From lines 3 to 9, we scan through the four quadrants of the CCCAS region and decide the main quadrant. The flipping of 2D matrix is performed in line 10 to transform the main quadrant to quadrant I as demonstrated in Fig. 5. For practical implementation, the flipping of 2D matrix can

---

Algorithm 1 Feature Compaction

Input: A $M \times N$ feature matrix X_0;
Output: Optimized feature vector $\boldsymbol{x_0}$;
1: Define $main\_quadrant = 1$ as the main quadrant;
2: Define $max\_sum = 0$ as the maximum summation;
3: **for** $index = 0$, $index < 4$, $index++$ **do**;
4:     Define $sum = $ summation of X_0 from column $index \times N/4$ to column $(index + 1) \times N/4$;
5:     **if** $sum > max\_sum$ **then**;
6:         $max\_sum = sum$;
7:         $main\_quadrant = index + 1$;
8:     **end if**
9: **end for**
10: Flip X_0 based on $main\_quadrant$;
11: Flatten X_0 into a vector $\boldsymbol{x_0}$ and return $\boldsymbol{x_0}$;

---

be achieved with simple column index switching. In line 11, the 2D feature matrix is flattened into a one-dimension (1D) feature vector for the classification model calibration. It shall be noted that, the illumination source symmetry-based feature compaction scheme can be easily extended to other symmetric scenarios, such as rotational symmetry. Overall, the feature extraction and compaction will yield a set of 1D feature vectors, e.g., $\{\boldsymbol{x_0}\}$, and each feature vector has an $M \times N$ dimension.

B. Model Training

With the SRAF labels and feature vectors, a classification model is calibrated for SRAF predictions. In particular, the size of training data set and feature vector dimension can both be very large because high sampling accuracy is needed for classification-based SRAF. We adopt logistic regression (LGR) and support vector classification with linear kernel (SVC) models for SRAF predictions, which demonstrate a promising trade-off between performance and runtime, compared to the model-based approach. We introduce the basic formulations, while detailed comparisons and analysis among different classification models are given in Section VI-A.

1) Logistic Regression: The LGR adopts the logistic function as the probabilistic estimation for each label of the training or testing data. The model calibration is typically achieved with the maximum likelihood method [26]. The detailed mathematical formulation is given as follows [27].

$$\min_{\boldsymbol{w}} \quad \boldsymbol{w}^T * \boldsymbol{w}/2 + C * \sum_i log(1 + exp(-y_i * \boldsymbol{w}^T * \boldsymbol{x_i})) \quad (1)$$

In Formulation (1), $\boldsymbol{w}$ is a vector of weight parameters for the logistic regression model, $\boldsymbol{x_i}$ and y_i are the extracted feature vector and SRAF label, respectively, for the ith training data sample, and C is the cost penalty for $L2$ regularization during an iterative optimization procedure. The LGR model is particularly powerful for binary classification, which makes the calibration and prediction scalable to large data sets. Due to the large training data set in classification-based SRAF issue, $L2$ regularization is added to the LGR model to avoid overfitting. The LGR model provides the direct probabilistic estimation of

labels for each data sample. For practical implementation, we adopt the logistic regression model from LIBLINEAR (related details can be found in [27]).

2) Support Vector Classification: Support vector classification (SVC) is a popular learning technique, which first decides a specified kernel, then maximizes the margin between the training data and decision boundary [28]. As a maximum margin classifier, SVC has been demonstrated to have several advantages over those classifiers maximizing some average quantity, such as LGR with maximum likelihood method [28]. In particular, SVC can better detect outliers (meaningless data), which can be easily removed with or without supervision [28]. This further generates a classification model with better accuracy for the SRAF generation problem. We adopt C-SVC formulation [28] with a linear kernel, which will show better learning accuracy and SRAF generation results than the simple LGR model. The detailed mathematical formulation is given as follows [29].

$$\min_{\boldsymbol{w},b,\xi} \quad \boldsymbol{w}^T * \boldsymbol{w}/2 + C * \sum_i \xi_i \quad (2)$$

$$\text{s.t.} \quad y_i * (\boldsymbol{w}^T * \boldsymbol{x_i} + b) \geq 1 - \xi_i \quad (C1)$$

$$\xi_i \geq 0, \quad \forall i \quad (C2)$$

In Formulation (2), $\boldsymbol{w}$ is a vector of weight parameters, $\boldsymbol{x_i}$ and y_i are the extracted feature vector and SRAF label, respectively, for the ith training data sample, C is the cost penalty for regularization against overfitting, b is the bias parameter for the linear hyperplane and ξ_i are a set of error parameters during model calibration (minimized in the objective function). For practical implementation, we adopt the SVC with linear kernel from LIBSVM (related details can be found in [29])

V. SRAF GENERATION

A. Predictions with Probability Maxima

The typical prediction with a binary classification model will be a label, i.e., 0 or 1, for each testing data. With the label prediction for each grid, clusters of grids will be labeled as 1, denoted as yellow grids, as shown in Fig. 6(a). After the label prediction, clusters of grids in Fig. 6(a) cannot be directly treated as SRAFs because they may violate the mask manufacturing rules or be printed due to large critical dimensions. Instead of using SRAF label for the grid prediction, we propose predictions with probability maxima to simplify the clusters of SRAF grids. When a classification model is calibrated, the probability of the label to be 1, denoted as p_1, can be calculated for LGR and SVC as explained in Section IV-B. With p_1 calculation at each grid point, a probability map on the 2D grid plane can be obtained as shown in Fig. 6(b). To simplify the clusters of grids for SRAF generation, we only insert SRAFs at grids with probability maxima. A grid with probability maximum means the probability (p_1) at that particular grid is larger than that at any other neighboring grids. The idea of predictions with probability maxima originates from the model-based SRAF approach. Model-based SRAFs

are generated using the guidance map from lithographic computations [10]–[13]. A guidance map is also grid based and has intensity assigned to each grid, where SRAFs will only be inserted at those intensity maxima. Thus, we adopt the similar idea during predictions with probability maxima since model-based SRAFs are used as the training data for the classification model calibration.
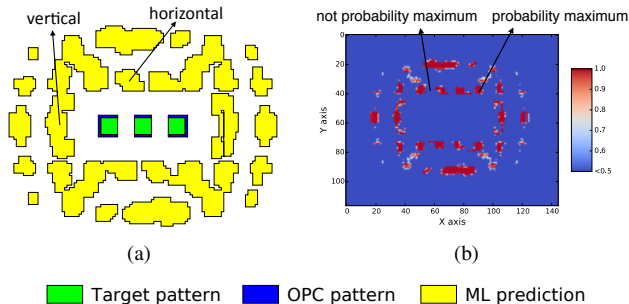

Fig. 6: SRAF predictions: (a) label predictions, (b) predictions with probability maxima.

B. SRAF Simplification

Using predictions with probability maxima, clusters of grids will be generated on the 2D grid plane but the mask manufacturing and SRAF printing issues are not fully resolved. The SRAF simplification phase aims at simplifying these clusters of grids into SRAFs satisfying the mask manufacturing rules, i.e., the max_width, min_space and max_length rules as mentioned in Section II-A. A greedy simplification scheme is proposed by grid merging and shrinking the SRAFs into rectangular shapes while accommodating mask manufacturing rules.

The overall algorithm of SRAF generation is shown in Algorithm 2. In lines 1-2, we predict SRAFs at grids with probability maxima from the classification model. In line 3, the grids with probability maxima are merged into polygons, which is followed by the spacing rule check and shrinking the polygons to remove violations in line 4. From line 5 to 14, each polygon is processed to generate a rectangular SRAF. Particularly, in line 7, the main direction of SRAF is detected based on the bounding box of target patterns. In line 8, the bounding box of the polygon is shrunk to achieve a rectangular SRAF parallel to that of target patterns. As illustrated in Fig. 6(a), the main direction of the polygon on the top is horizontal while the main direction on the left is vertical, both of which are parallel to the bounding box of target patterns. With the SRAF simplification, the mask manufacturing-friendly SRAFs can be generated for testing patterns.

VI. EXPERIMENTAL RESULTS

We have implemented the supervised data learning techniques in C++ and all experiments are performed on an 8-core Linux machine with 3.4GHz Intel(R) Core and 32GB memory. The logistic regression (LGR) and support vector classification (SVC) with linear kernel models are based on LIBLINEAR [27] and LIBSVM [29], respectively. For the

---

Algorithm 2 SRAF generation

Input: A 2D grid plane, a classification models, a set of mask manufacturing rules;
Output: The mask manufacturing friendly set $SRAF$;
1: Compute the probability of label 1 for each grid;
2: SRAF predictions at grids with probability maxima;
3: Merge SRAF grids into a polygon set $SRAF_{pg}$;
4: Spacing rule check and shrink polygons in $SRAF_{pg}$ to remove violations;
5: **for** each $polygon$ in $SRAF_{pg}$ **do**;
6:     Define $BBox$ as the bounding box of $polygon$;
7:     Detect the main direction of $polygon$ as $direction$;
8:     Shrink $BBox$ size based on $direction$;
9: **end for**
10: Rule check and shrink rectangles in $SRAF$ to remove violations;
11: Return $SRAF$;

LGR model, C is set to 0.1 and the stopping accuracy is set to 10^{-9}. For the SVC model, C is set to 0.02 and the stopping accuracy is set to 10^{-9}. The optical model, model-based SRAF, MRC/LCC recipes and the SRAF simplification are implemented using Calibre script language with the industry-strength setup. The model-based SRAFs are computed from coherence maps generated with inverse Lithography. For the optical model, the wavelength (λ) and numerical aperture (NA) are set as $193nm$ and 1.35, respectively. The annular illumination source is used with outer sigma as 0.9 and inner sigma as 0.6. Compact model 1 from Calibre is adopted as the resist model. In the LCC, the outer/inner contours are generated using lithographic process window conditions with a focus variation of $\pm 30nm$ and a dose variation of $\pm 3.0\%$. The nominal contours are generated at the best {focus, dose} conditions. For model-based SRAF generation, process window conditions above are considered and SRAF manufacturing rules are set as max_width = $40nm$, min_space = $60nm$, max_length = $90nm$. For the SRAF label of each grid, it is discretized into 0 or 1 based on the coverage of rectangular SRAFs over that particular grid. The coverage threshold is set to 25%, empirically.

We test the SRAF generation framework on two types of contact patterns. One type is dense contact arrays with contact width and space fixed as $70nm$. We have dense contact patterns because redundant vias are needed to improve yield during layout design. The other type is sparse contact patterns, where the contact width is $70nm$ but the space between contact holes is random and the minimum space is $70nm$. For CCCAS, the grid size is set as $10nm$, the SRAF box size is set as $40nm$ and radius step size is s_r =$15nm$. The grid size is chosen empirically to balance the accuracy and runtime from SRAF generation. For SRAF-specific constraints, d_{opc} and d_{sraf} are set as $100nm$ and $600nm$, respectively.

A. Training Data

A set of training patterns and model-based SRAFs are needed to extract the training data and calibrate the classification model for SRAF predictions on both dense and

sparse testing patterns. From the extensive experiments, the training patterns in Fig. 7 yield the best training and testing accuracy. For the dense contact arrays in Fig. 7(a), the width and space are fixed as $70nm$. For the random contact patterns in Fig. 7(b), the width is $70nm$, the space between contacts are random and the minimum space is $70nm$. The width of sparse contact arrays in Fig. 7(c) is $70nm$, while the space is $350nm$. In particular, since the training patterns are symmetric and feature compaction scheme has been proposed, we only need to sample the lower left part of the layout clip for symmetric training data in Fig 7(a) and Fig 7(c). This is beneficial for the classification model calibration since the training data size can be reduced by 3/4 without losing the critical SRAF information.
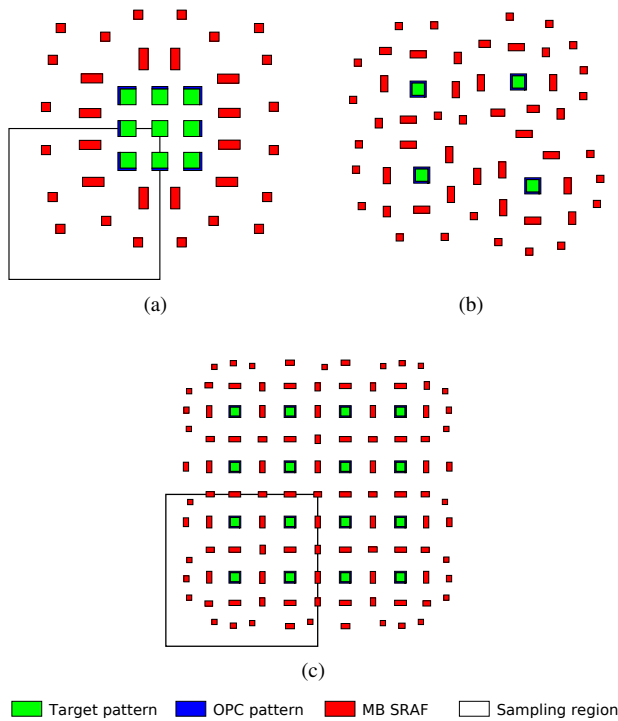

Fig. 7: Training layout: (a) dense contact arrays, (b) random contact patterns, (c) sparse contact arrays.

We select two training data sets for model training and validation. "Training set 1" consists of the extracted samples from the layout in Fig. 7(a) and Fig. 7(c).[1] "Training set 2" includes the extracted samples from the layout in Fig. 7(a) and Fig. 7(b). The training data set statistics are summarized in Table I. For CCCAS, the number of circles is set as $M = \lfloor (d_{sraf} - d_{opc})/s_r \rfloor = 33$. The number of sub-sampling points in each circle is set as $N = 32$ to guarantee sampling accuracy for sparse contact patterns. Then, the feature vector dimension is $M \times N = 1056$. In Table I, we have 13378 and 24298 samples for "Training set 1" and "Training set 2",

---

[1] The conference version [1] only adopts "Training set 1" for experimental validations.

TABLE I: Data set statistics

Feature vector dimension	1056
# of samples from training set 1	13378
# of samples from training set 2	24298
# of testing samples from dense patterns	86000
# of testing samples from sparse patterns	873991

respectively. In addition, we have 86000 and 873991 testing samples from dense and sparse patterns, respectively.

The data set statistics demonstrate the high feature vector dimension and large training data size. The feature vector dimension is difficult to be further reduced since each sub-sampling point contains the information related to the target patterns. Moreover, each training data sample within the lithographic interaction window is considered valuable, so there is little redundancy within the training data set.

B. Model Training

We compare different classification models, including LGR and SVC, for the SRAF generation framework and data statistics are shown in Table II. The runtime ("T(s)") is evaluated in seconds. The model accuracy (training and testing) is evaluated using confusion matrix [30]. True positive (TP) and false negative (FN) are defined as the number of correctly (1's) and incorrectly (0's) predicted labels for real positive labels (1's) in the data. Similarly, true negative (TN) and false positive (FP) are defined as the number of correctly (0's) and incorrectly (1's) predicted labels for real negative labels (0's) in the data. This further defines the following accuracy metrics for training and testing:

$$\text{TPR} = TP/(TP+FN) \qquad \text{TNR} = TN/(TN+FP)$$
$$\text{FNR} = FN/(FN+TP) \qquad \text{FPR} = FP/(FP+TN)$$
$$\text{Accuracy} = (TP+TN)/(TP+TN+FP+FN)$$

where "TPR", "TNR" and "Accuracy" are best at 1.0 (worst at 0.0), while "FNR" and "FPR" are best at 0.0 (worst at 1.0) for comparisons.

Table II demonstrates that SVC model consistently obtains much better "TNR" and "FPR" than the LGR model, across training and testing with both "Training set 1" and "Training set 2". However, the LGR model can deliver better "TPR" and "FNR" than the SVC model, except the training stage using "Training set 1". In general, for the SRAF generation problem, the number of positive-labeled real data is much less than the negative-labeled real data. This is because SRAFs are very small features and can only be inserted at certain locations, i.e., those grids benefiting the printing of target patterns. This means "TNR" and "FPR" have much larger weight than the "TPR" and "FNR" for the overall "Accuracy". This further explains the SVC model consistently achieves much better overall "Accuracy" than the LGR model. Although the testing runtime is similar, the SVC model introduces much larger training runtime than the LGR model, especially for "Training set 2", but it is affordable for one-time computation.

This article has been accepted for publication in a future issue of this journal, but has not been fully edited. Content may change prior to final publication. Citation information: DOI 10.1109/TCAD.2017.2748029, IEEE Transactions on Computer-Aided Design of Integrated Circuits and Systems

IEEE TRANSACTIONS ON COMPUTER-AIDED DESIGN OF INTEGRATED CIRCUITS AND SYSTEMS, VOL. , NO. 8

TABLE II: Comparisons on different classification models

		Metric	LGR	SVC
Training set 1	Training	TPR	1.0000	1.0000
		FNR	0.0000	0.0000
		FPR	0.0542	0.0173
		TNR	0.9458	0.9827
		Accuracy	0.9495	0.9839
		T(s)	0.82	48.7
	Dense testing patterns	TPR	0.5057	0.3363
		FNR	0.4943	0.6637
		FPR	0.1581	0.0769
		TNR	0.8419	0.9231
		Accuracy	0.8256	0.8945
		T(s)	0.09	0.05
	Sparse testing patterns	TPR	0.3362	0.2379
		FNR	0.6638	0.7621
		FPR	0.1625	0.0923
		TNR	0.8375	0.9077
		Accuracy	0.7936	0.8490
		T(s)	1.28	0.44
Training set 2	Training	TPR	0.9781	0.2337
		FNR	0.0219	0.7663
		FPR	0.1436	0.0068
		TNR	0.8564	0.9932
		Accuracy	0.8637	0.9476
		T(s)	1.55	799.7
	Dense testing patterns	TPR	0.5330	0.2261
		FNR	0.4670	0.7739
		FPR	0.1916	0.0489
		TNR	0.8084	0.9511
		Accuracy	0.7950	0.9158
		T(s)	0.1	0.13
	Sparse testing patterns	TPR	0.3354	0.1610
		FNR	0.6646	0.8390
		FPR	0.1487	0.0585
		TNR	0.8513	0.9415
		Accuracy	0.8061	0.8731
		T(s)	1.19	1.29

C. SRAF Generation

1) SRAF Simplification: We demonstrate the strength of predictions with probability maxima and SRAF simplification schemes. As illustrated in Fig. 8, we compare the SRAFs generated using different machine learning (ML) predictions, i.e. label predictions and predictions with probability maxima, followed by the SRAF simplification phase. Predictions with probability maxima can simplify the clusters of grids labeled as 1, i.e. breaking large clusters into small clusters, which benefits the SRAF simplification stage. Thus, the SRAFs generated using predictions with probability maxima in Fig. 8(b) are much better than those in Fig. 8(a) in terms of PV band from the LCC.

2) SRAF Consistency: We further demonstrate the benefit of SRAF consistency improvement from the feature compaction technique in Section IV-A2. The SRAF generation from the model-based method using Calibre [Calibre, v2015.2_36.27], LGR without feature compaction and LGR with feature compaction are shown in Fig. 9(a), 9(b) and 9(c), respectively. Since annular illumination source is used, axial symmetric grids share the same optical environment and the consistent SRAF generation should yield the same SRAFs at axial symmetric grids. The feature compaction scheme would transform the feature matrices extracted from axial symmetric grids to
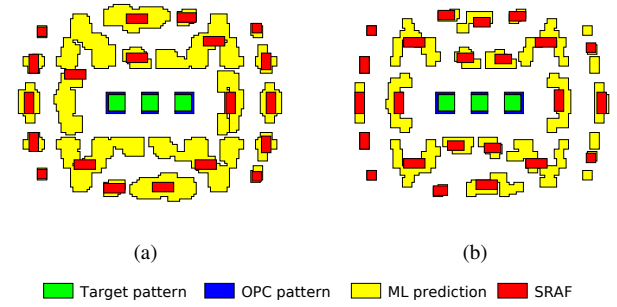

Fig. 8: SRAF generations: (a) label predictions, (b) predictions with probability maxima.

the same feature vector. Therefore, the SRAFs in Fig. 9(c) are more consistent than those in Fig. 9(b). Moreover, we have even achieved SRAFs with better consistency than the model-based method shown in Fig. 9(a). This is because model-based method first generates a set of guidance maps from lithographic calculations. The manufacturability of the SRAFs is further considered with heuristic rectangle insertions, where the consistency is very difficult to be addressed. For the proposed ML-based approach, axial symmetric grids share the same feature vectors, which further lead to symmetric, i.e., consistent, ML predictions if we assume the grid error is negligible.
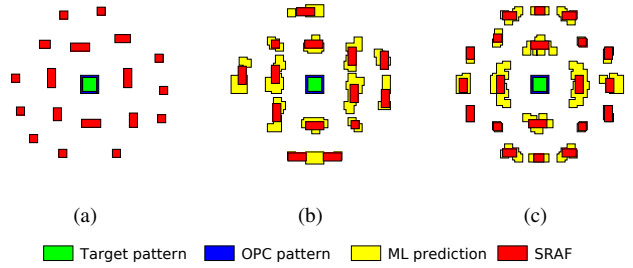

Fig. 9: SRAFs for the isolated contact pattern: (a) model-based, (b) LGR without feature compaction, (c) LGR with feature compaction.

We demonstrate the SRAFs from SVC-based predictions on dense and sparse testing patterns as shown in Fig. 10. The SRAF predictions using "Training set 1" and "Training set 2" are shown in Fig. 10(a) and Fig. 10(b), respectively. The left and middle patterns show two cases of redundant vias in real designs. The SVC-based SRAF generation can obtain acceptable SRAFs on these dense contact patterns but the degradation of SRAF consistency is observed, especially for "Training set 2". The reasons are twofold. First, the training data with model-based SRAFs are not perfectly consistent as shown in Fig. 7. Then, it is difficult to guarantee the consistent SRAF generation with the classification model calibrated with these training data. In particular, "Training set 2" includes random contact patterns in Fig. 7(b), where SRAF consistency is not explicitly included. This further leads to degraded SRAF

(a)

(b)

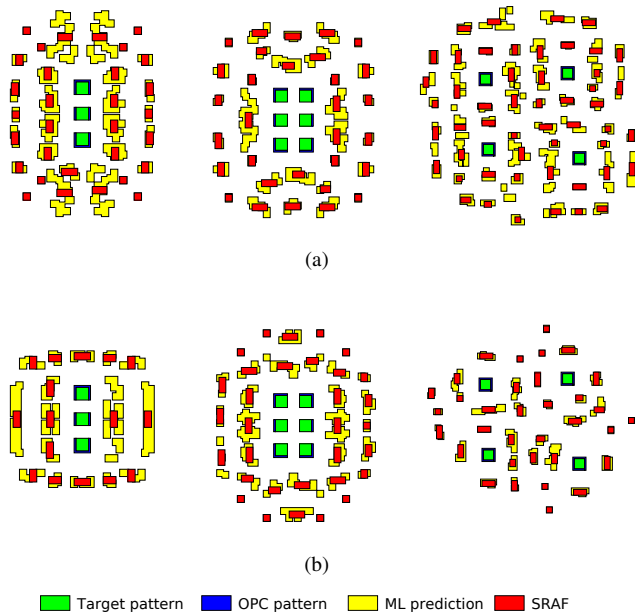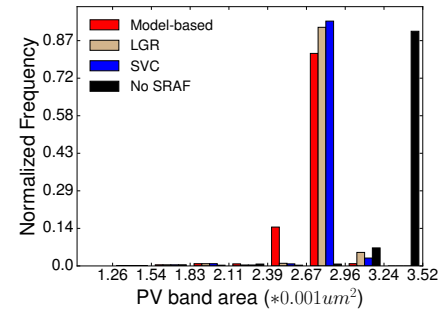| Target pattern | OPC pattern | ML prediction | SRAF |

Fig. 10: SVC with linear kernel model predictions on contact patterns, including dense contact patterns (left and middle) and sparse contact patterns(right): (a) using "Training set 1", (b) using "Training set 2".

(a)

(b)

Fig. 11: Comparison among different schemes in terms of PV band distribution: (a) using "Training set 1", (b) using "Training set 2".
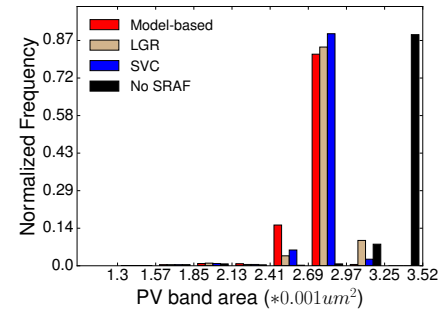
consistency for the contact patterns on the left of Fig. 10(b). Second, the CCCAS results may be slightly different for axial symmetric grids due to the grid error within the 2D grid plane. The contact patterns on the right of Fig. 10(a) and Fig. 10(b) illustrate a small layout clip of random contact patterns, which proves the capability of the machine learning-based SRAF generation on random sparse contact patterns. However, the SRAF generation results, i.e., shapes and locations of SRAFs, highly depend on the training data. This means the performance of the SRAF generation results needs to be evaluated in a complete mask optimization flow.

D. Lithography Compliance Check

To evaluate the practical lithographic performance, we combine the SRAF generation with a complete mask optimization flow as shown in Fig. 2, where model-based OPC and LCC are performed using Mentor Calibre tool. We compare the model-based, LGR and SVC approach in terms of PV band and EPE on both dense and sparse testing patterns. Specifically, we collect the PV band value for each contact and the EPE value at the center of the four edges of each contact at nominal conditions. The mean values are summarized and compared in Table III. We add the PV band without SRAFs to better demonstrate the benefit from SRAF generation. The model-based approach reduces the PV band from 3.3029 to 2.7685, which is 16.18% reduction compared to no SRAF insertion. Meanwhile, for "Training set 1", we obtain 13.72% and 14.08% PV band reduction from LGR and SVC, respectively. For "Training set 2", we achieve 13.97% and 14.87% PV band reduction from LGR and SVC, respectively. Thus, the SVC model achieves

better performance than the LGR model for SRAF generation, especially when using "Training set 2". In particular, there is only 1.31% PV band degradation from model-based approach to the SVC-based approach with "Training set 2". We take the absolute values when calculating the EPE mean to avoid the cancellations between positive and negative values of EPE. The LGR-based and SVC-based SRAF generation yield the smallest EPE mean value with "Training set 1" and "Training set 2", respectively. They both outperform the model-based approach in terms of the EPE mean value. This means there is some trade-off between PV band and EPE because different SRAF results lead to different OPC results. It is very difficult to improve the PV band and EPE simultaneously with a robust mask optimization flow.

We collect the PV band and EPE values for each contact and further plot the data in histograms as shown in Fig. 11 and Fig. 12. Fig. 11 shows that SRAF insertion significantly improves the PV band, compared to no SRAF insertion, and model-based SRAF gives the best performance. The SVC-based approach is slightly worse than model-based method but performs better than LGR-based method, across different training data sets. Fig. 12(a) and Fig. 12(b) show that LGR-based and SVC-based SRAF generations achieve the best EPE performance, using "Training set 1" and "Training set 2", respectively. This generates an important empirical observation that training data selection is very important for the SRAF generation with supervised data learning. Our extensive experiments demonstrate much better accuracy and lithographic performance from the SVC model, but it only happens when

TABLE III: PV band and absolute of EPE

			Training data set 1		Training data set 2	
Mean value	No SRAF	Model-based	LGR	SVC	LGR	SVC
PV band ($.001um^2$)	3.3029	2.7685	2.8496	2.8380	2.8416	2.8117
Absolute of EPE (nm)	3.6343	0.5427	0.4861	0.4938	0.4938	0.4692

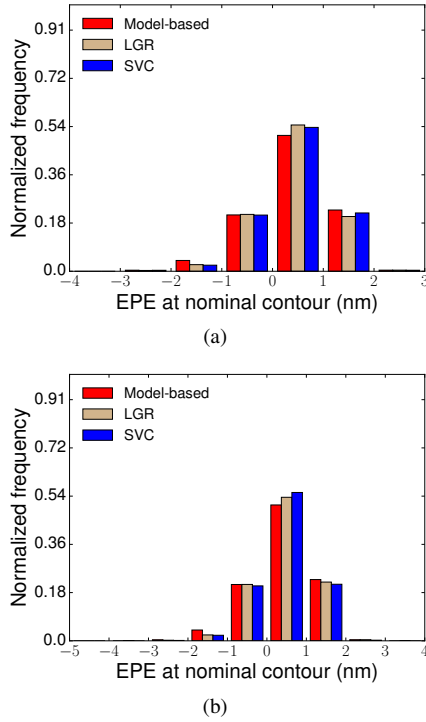
Fig. 12: Comparison among different schemes in terms of EPE distribution at nominal conditions: (a) using "Training set 1", (b) using "Training set 2".

Fig. 13: Runtime comparison among different schemes on different layout windows: (a) using "Training set 1", (b) "using training set 2".

combined with "Training set 2". We treat advanced training data selection as our important future work for the SRAF generation problem.

E. Runtime

We compare the machine learning-based SRAF generation with the commercial Calibre tool, i.e. model-based SRAFs. The mask optimization techniques, including SRAF generation and OPC, usually apply to small layout windows due to the high computational cost [3]. To demonstrate the scalability of the proposed approach, we choose layout clips as large as $100um^2$ in area for runtime comparisons among different SRAF generation approaches. In Fig. 13(a) and Fig. 13(b), different contact patterns, denoted as $m \times n$ (width $\times$ height of the layout clip), are used for runtime comparisons. The areas of these layout windows considering SRAF regions are in the range from $1um^2$ to $100um^2$. The runtime for the machine learning-based approach includes runtime for feature extraction and compaction, predictions with probability maxima and SRAF simplification. The model calibration time is not included since it is one-time computation.
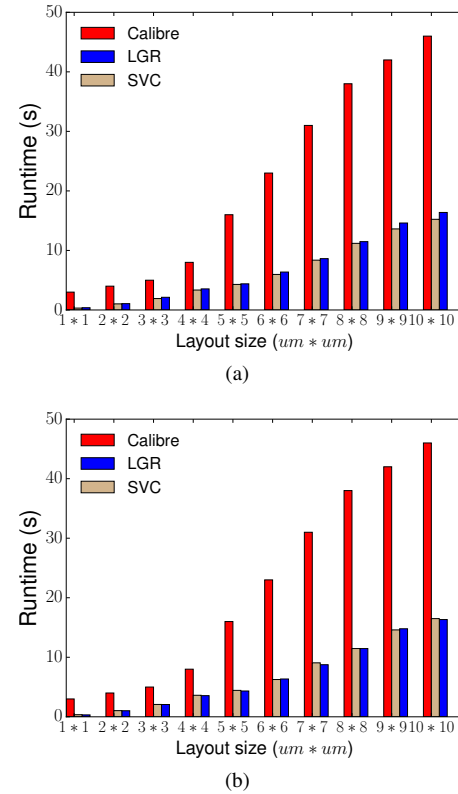
Although we are using a different database and algorithm implementation from the commercial tool, in a lithographic window (1-$2um^2$), we obtain over 10X speed-up from the machine learning-based SRAF generation, compared to the model-based approach in Calibre [Calibre, v2014.4_18.13]. For the largest layout clip ($100um^2$), we still achieve over 3X speed-up compared to the model-based approach. The significant runtime speed-up aforementioned is consistent, across different learning models (SVC and LGR) and training data sets, as shown in Fig. 13(a) and Fig. 13(b). The SRAF generation is combined with model-based OPC from Calibre to achieve an entire mask optimization flow. Since different SRAFs may lead to different model-based OPC behaviors, we also check the runtime of the model-based OPC from different SRAF generation approaches and ensure that they are approximately the same. Since the lithographic performance of the SVC model is better than the LGR model and they have similar SRAF generation runtime, the SVC model proves to be the better classification model for SRAF generation.

VII. Conclusion

The SRAF generation with supervised data learning is demonstrated for the first time. A robust feature extraction scheme is proposed by adapting the concentric circle with area sampling considering SRAF-specific constraints. We further propose a novel feature compaction technique based on the illumination source symmetry to reduce the training data size and improve the SRAF consistency. The LGR and SVC models are adopted for scalable model training and testing. Instead of using conventional label predictions with a classification model, predictions with probability maxima are proposed to achieve mask manufacturing-friendly SRAFs. Compared to the commercial Calibre tool, the SVC-based SRAF generation obtains 10X speed-up in layout windows and over 3X speed-up for a $100um^2$ layout clip. The SVC-based SRAF generation also achieves much better EPE and affordable degradation (1.31%) in PV band, compared to the commercial Calibre tool.

Our future work includes advanced training data selection techniques and learning models for better SRAF generations.

VIII. Acknowledgement

References

[1] X. Xu, T. Matsunawa, S. Nojima, C. Kodama, T. Kotani, and D. Z. Pan, "A Machine Learning Based Framework for Sub-Resolution Assist Feature Generation," in *ACM International Symposium on Physical Design (ISPD)*, 2016, pp. 161–168.

[2] Y. Ping, S. McGowan, Y. Gong, Y. M. Foong, J. Liu, J. Qiu, V. Shu, B. Yan, J. Ye, P. Li *et al.*, "Process window enhancement using advanced ret techniques for 20nm contact layer," in *Proc. of SPIE*, 2014, pp. 90 521N–90 521N.

[3] S. Banerjee, Z. Li, and S. R. Nassif, "ICCAD-2013 CAD contest in mask optimization and benchmark suite," in *IEEE/ACM International Conference on Computer-Aided Design (ICCAD)*, 2013, pp. 271–274.

[4] J.-R. Gao, X. Xu, Y. Bei, and D. Z. Pan, "MOSAIC: Mask optimizing solution with process window aware inverse correction," in *ACM/IEEE Design Automation Conference (DAC)*, 2014, pp. 52:1–52:6.

[5] Y.-H. Su, Y.-C. Huang, L.-C. Tsai, Y.-W. Chang, and S. Banerjee, "Fast lithographic mask optimization considering process variation," in *IEEE/ACM International Conference on Computer-Aided Design (ICCAD)*, 2014, pp. 230–237.

[6] A. Awad, A. Takahashi, S. Tanaka, and C. Kodama, "A fast process variation and pattern fidelity aware mask optimization algorithm," in *IEEE/ACM International Conference on Computer-Aided Design (ICCAD)*, 2014, pp. 238–245.

[7] J. Kuang, W.-K. Chow, and E. F. Young, "A robust approach for process variation aware mask optimization," in *Proc. Design, Automation and Test in Eurpoe*, 2015, pp. 1591–1594.

[8] J.-H. Jun, M. Park, C. Park, H. Yang, D. Yim, M. Do, D. Lee, T. Kim, J. Choi, G. Luk-Pat *et al.*, "Layout optimization with assist features placement by model based rule tables for 2x node random contact," in *Proc. of SPIE*, 2015, pp. 94 270D–94 270D.

[9] C. Kodama, T. Kotani, S. Nojima, and S. Mimotogi, "Sub-resolution assist feature arranging method and computer program product and manufacturing method of semiconductor device," Aug. 19 2014, US Patent 8,809,072.

[10] K. Sakajiri, A. Tritchkov, and Y. Granik, "Model-based sraf insertion through pixel-based mask optimization at 32nm and beyond," in *Proc. of SPIE*, 2008, pp. 702 811–702 811.

[11] R. Viswanathan, J. T. Azpiroz, and P. Selvam, "Process optimization through model based sraf printing prediction," in *Proc. of SPIE*, 2012, pp. 83 261A–83 261A.

[12] J. Ye, Y. Cao, and H. Feng, "System and method for model-based sub-resolution assist feature generation," Feb. 1 2011, US Patent 7,882,480.

[13] S. D. Shang, L. Swallow, and Y. Granik, "Model-based sraf insertion," Oct. 11 2011, US Patent 8,037,429.

[14] L. Pang, Y. Liu, and D. Abrams, "Inverse lithography technology (ilt): a natural solution for model-based sraf at 45nm and 32nm," in *Proc. of SPIE*, 2007, pp. 660 739–660 739.

[15] B.-S. Kim, Y.-H. Kim, S.-H. Lee, S.-I. Kim, S.-R. Ha, J. Kim, and A. Tritchkov, "Pixel-based sraf implementation for 32nm lithography process," in *Proc. of SPIE*, 2008, pp. 71 220T–71 220T.

[16] J. A. Torres, "ICCAD-2012 CAD contest in fuzzy pattern matching for physical verification and benchmark suite," in *IEEE/ACM International Conference on Computer-Aided Design (ICCAD)*, 2012.

[17] D. Ding, X. Wu, J. Ghosh, and D. Z. Pan, "Machine learning based lithographic hotspot detection with critical-feature extraction and classification," in *IEEE International Conference on IC Design and Technology (ICICDT)*, 2009.

[18] D. G. Drmanac, F. Liu, and L.-C. Wang, "Predicting variability in nanoscale lithography processes," in *ACM/IEEE Design Automation Conference (DAC)*, 2009, pp. 545–550.

[19] Y. Yu, G. Lin, I. Jiang, and C. Chiang, "Machine-learning-based hotspot detection using topological classification and critical feature extraction," *IEEE Transactions on Computer-Aided Design of Integrated Circuits and Systems (TCAD)*, vol. 34, no. 3, pp. 460–470, 2015.

[20] T. Matsunawa, J.-R. Gao, B. Yu, and D. Z. Pan, "A new lithography hotspot detection framework based on adaboost classifier and simplified feature extraction," in *Proc. of SPIE*, 2015, pp. 94 270S–94 270S.

[21] A. Gu and A. Zakhor, "Optical proximity correction with linear regression," *IEEE Transactions on Semiconductor Manufacturing*, vol. 21, no. 2, pp. 263–271, 2008.

[22] R. Luo, "Optical proximity correction using a multilayer perceptron neural network," *Journal of Optics*, vol. 15, no. 7, p. 075708, 2013.

[23] T. Matsunawa, B. Yu, and D. Z. Pan, "Optical proximity correction with hierarchical bayes model," in *Proc. of SPIE*, 2015, pp. 94 260X–94 260X.

[24] X. Ma, B. Wu, Z. Song, S. Jiang, and Y. Li, "Fast pixel-based optical proximity correction based on nonparametric kernel regression," *Journal of Microlithography, Microfabrication and Microsystems*, vol. 13, no. 4, pp. 043 007–043 007, 2014.

[25] P. Gupta, "What is process window?" *SIGDA Newsl.*, vol. 40, no. 8, pp. 1–1, Aug. 2010.

[26] T. Hastie, R. Tibshirani, J. Friedman, and J. Franklin, "The elements of statistical learning: data mining, inference and prediction," *The Mathematical Intelligencer*, vol. 27, no. 2, pp. 83–85, 2005.

[27] R.-E. Fan, K.-W. Chang, C.-J. Hsieh, X.-R. Wang, and C.-J. Lin, "LIBLINEAR: A library for large linear classification," *Journal of machine learning research*, vol. 9, no. Aug, pp. 1871–1874, 2008.

[28] B. E. Boser, I. M. Guyon, and V. N. Vapnik, "A training algorithm for optimal margin classifiers," in *Proceedings of the fifth annual workshop on Computational learning theory*. ACM, 1992, pp. 144–152.

[29] C.-C. Chang and C.-J. Lin, "LIBSVM: A library for support vector machines," *ACM Transactions on Intelligent Systems and Technology*, vol. 2, pp. 27:1–27:27, 2011, software available at http://www.csie.ntu.edu.tw/~cjlin/libsvm.

[30] D. M. Powers, "Evaluation: from precision, recall and f-measure to roc, informedness, markedness and correlation," 2011.

This article has been accepted for publication in a future issue of this journal, but has not been fully edited. Content may change prior to final publication. Citation information: DOI 10.1109/TCAD.2017.2748029, IEEE Transactions on Computer-Aided Design of Integrated Circuits and Systems

IEEE TRANSACTIONS ON COMPUTER-AIDED DESIGN OF INTEGRATED CIRCUITS AND SYSTEMS, VOL. , NO. 12

Xiaoqing Xu (S'15-M'17) received the B.S. degree in microelectronics from Peking University, Beijing, China, in 2012 and the M.S.E. and Ph.D. degrees in electrical and computer engineering from the University of Texas at Austin, in 2015 and 2017, respectively. He is now with ARM Research, Austin, TX, as a Senior Research Engineer. His research interests include robust standard cell design, design for manufacturability and physical design.

His research has been recognized with numerous awards including Golden Medal at ACM Student Research Competition at ICCAD 2016, University Graduate Continuing Fellowship in 2016, SPIE BACUS Fellowship in 2016, Best in Session Award at SRC TECHCON 2015, William J. McCalla Best Paper Award at ICCAD 2013 and CAD Contest Award at ICCAD 2013.

Yibo Lin received the B.S. degree from Shanghai Jiaotong University, Shanghai, China, in 2013, and his M.S. degree from University of Texas at Austin in 2017. He is currently pursuing the Ph.D. degree at the Department of Electrical and Computer Engineering, University of Texas at Austin. His research interests include physical design and design for manufacturability.

He has received Franco Cerrina Memorial Best Student Paper Award at SPIE Advanced Lithography Conference 2016, and National Scholarship at Shanghai Jiaotong University in 2012. He has interned at Toshiba, IMEC, Cadence, and Oracle.

Meng Li (S'16) received his B.S. degree in Microelectronics from Peking University, Beijing, China in 2013. He is currently pursuing the Ph.D degree in Electrical and Computer Engineering, University of Texas at Austin, under the supervision of Prof. David Z. Pan. His research interests include hardwareoriented security, reliability and power grid simulation acceleration. He received best paper award in HOST 2017 and Graduate Fellowship from UT Austin in 2013.

Tetsuaki Matsunawa received his Ph.D. degree in computer science from the University of Tsukuba, Tsukuba, Japan in 2008. He joined Toshiba Corporation in 2008 and has been working in the area of optical lithography. He visited the University of Texas at Austin as a visiting scholar from 2013 to 2015. His current research interests include design for manufacturability and machine learning algorithms with applications in computational lithography.

Shigeki Nojima received the B.S. degree in geoscience and the M.S. degree in mineralogy from the University of Tokyo, Tokyo, Japan, in 1992 and 1994, respectively. Since 1994, he has been at Toshiba Corporation, Yokohama, Japan, where he was engaged in development of lithography and Technology CAD, especially process simulation, optical proximity correction, design for manufacturability, and CAD for emerging lithography. He has published over 30 technical papers in international conference proceedings and journals and holds over 30 U.S. patents.

Mr. Nojima was a recipient of the Best Paper Award in the Ninth and Tenth Symposium on Photomask and Next-Generation Lithography Mask Technology in 2002 and 2003, respectively. He was a technical program committee member of Design for Manufacturability and Reliability in IEEE/ACM Asia and South Pacific Design Automation Conference from 2013 to 2015. He has been a program committee of Design-Process-Technology Co-optimization for Manufacturability in International Society for Optics and Photonics (SPIE) Advanced Lithography since 2014. He is a member of the SPIE.

Chikaaki Kodama (S'04–M'06–SM'12) received the B.E., M.E., and D.E. degrees in electronic and information engineering from Tokyo University of Agriculture and Technology, Tokyo, Japan, in 1999, 2001, and 2006, respectively.

He was at the Development of Custom Computer-Aided Design for SPARC64 Processor, Fujitsu Ltd., Kawasaki, Japan, from 2001 to 2003. He is currently with Toshiba Memory Corporation, Yokohama, Japan. His current research interests include design for manufacturability, especially mask optimization for optical lithography, and very large scale integration layout design. He has published about 50 technical papers in international conference proceedings and journals. He holds about 30 Japan, China, and U.S. patents. Dr. Kodama is a senior member of IEEE

Toshiya Kotani received the B.E. and M.E. degrees in materials science and engineering from Waseda University, Tokyo, Japan, in 1994 and 1996, respectively. Since 1996, he has been at Toshiba Corporation, Yokohama, Japan, where he was engaged in the development of lithography, optical proximity correction, and design for manufacturability technologies for memory device. Since 2012, he has been the Manager of Memory Lithography Group of Memory Design Department, responsible for lithography technology for leading-edge NAND flash memory design. He has published over 30 technical papers in international conference proceedings and journals and holds over 100 Japan and U.S. patents.

Mr. Kotani was the recipient of the Best Paper Award in the Tenth Symposium on Photomask and Next-Generation Lithography Mask Technology in 2003.

David Z. Pan (S'97–M'00–SM'06-F'14) received his B.S. degree from Peking University, and his M.S. and Ph.D. degrees from University of California, Los Angeles (UCLA). From 2000 to 2003, he was a Research Staff Member with IBM T. J. Watson Research Center. He is currently the Engineering Foundation Endowed Professor at the Department of Electrical and Computer Engineering, The University of Texas at Austin. He has published over 250 papers in refereed journals and conferences, and is the holder of 8 U.S. patents. His research interests include cross-layer nanometer IC design for manufacturability, reliability, security, new frontiers of physical design, and CAD for emerging technologies.

He has served as a Senior Associate Editor for ACM Transactions on Design Automation of Electronic Systems (TODAES), an Associate Editor for IEEE Design & Test, IEEE Transactions on Computer Aided Design of Integrated Circuits and Systems (TCAD), IEEE Transactions on Very Large Scale Integration Systems (TVLSI), IEEE Transactions on Circuits and Systems PART I (TCAS-I), IEEE Transactions on Circuits and Systems PART II (TCAS-II), Science China Information Sciences (SCIS), Journal of Computer Science and Technology (JCST), etc. He has served as Program/General Chair of ISPD 2007/2008, TPC Chair for ASPDAC 2016, Vice Program Chair for ICCAD 2017, Tutorial Chair for DAC 2014, among others.

He has received a number of awards, including the SRC 2013 Technical Excellence Award, DAC Top 10 Author in Fifth Decade, DAC Prolific Author Award, ASPDAC Frequently Cited Author Award, 13 Best Paper Awards and several international CAD contest awards, Communications of the ACM Research Highlights (2014), ACM/SIGDA Outstanding New Faculty Award (2005), NSF CAREER Award (2007), SRC Inventor Recognition Award three times, IBM Faculty Award four times, UCLA Engineering Distinguished Young Alumnus Award (2009), and UT Austin RAISE Faculty Excellence Award (2014).